ACCURATE WAVELENGTH MEASUREMENTS AND MODELING OF Fe xv TO Fe xix SPECTRA RECORDED IN HIGH-DENSITY PLASMAS BETWEEN 13.5 AND 17 Å

M. J. May, P. Beiersdorfer, J. Dunn, N. Jordan, S. B. Hansen, and A. L. Osterheld

L-260, Lawrence Livermore National Laboratory, Livermore, CA 94551; may13@llnl.gov

A. Ya. Faenov, T. A. Pikuz, and I. Yu. Skobelev

Multicharged Ions Spectra Data Center of VNIIFTRI, Moscow region, 141570, Russia

F. Flora, S. Bollanti, P. Di Lazzaro, and D. Murra

ENEA, Dipartimento Innovazione, Settore Fisica Applicata, 00044 Frascati, Rome, Italy

A. Reale, L. Reale, G. Tomassetti, and A. Ritucci

Dipartimento di Fisica e INFN g.s. INGS, Università de L'Aquila, 67010 L'Aquila, Italy

AND

M. Francucci, S. Martellucci, and G. Petrocelli

INFM—Dipartimento di Science e Tecnologie Fisiche ed Energetiche, Università di Roma Tor Vergata,
Via di Tor Vergata, 00133 Rome, Italy

Received 2004 October 11; accepted 2005 February 7

ABSTRACT

Iron spectra have been recorded from plasmas created at three different laser plasma facilities: the Tor Vergata University laser in Rome (Italy), the Hercules laser at ENEA in Frascati (Italy), and the Compact Multipulse Terawatt (COMET) laser at LLNL in California (USA). The measurements provide a means of identifying dielectronic satellite lines from Fe xvi and Fe xv in the vicinity of the strong $2p \rightarrow 3d$ transitions of Fe xvii. About 80 $\Delta n \geq 1$ lines of Fe xv (Mg-like) to Fe xix (O-like) were recorded between 13.8 and 17.1 Å with a high spectral resolution ($\lambda/\Delta\lambda \approx 4000$); about 30 of these lines are from Fe xvi and Fe xv. The laser-produced plasmas had electron temperatures between 100 and 500 eV and electron densities between 10^{20} and 10^{22} cm^{-3}. The Hebrew University Lawrence Livermore Atomic Code (HULLAC) was used to calculate the atomic structure and atomic rates for Fe xv–xix. HULLAC was used to calculate synthetic line intensities at $T_e = 200$ eV and $n_e = 10^{21}$ cm^{-3} for three different conditions to illustrate the role of opacity: optically thin plasmas with no excitation-autoionization/dielectronic recombination (EA/DR) contributions to the line intensities, optically thin plasmas that included EA/DR contributions to the line intensities, and optically thick plasmas (optical depth $\approx$200 μm) that included EA/DR contributions to the line intensities. The optically thick simulation best reproduced the recorded spectrum from the Hercules laser. However, some discrepancies between the modeling and the recorded spectra remain.

Subject headings: atomic data — methods: laboratory

1. INTRODUCTION

The characteristics of hot astrophysical plasmas are deduced from precise X-ray spectroscopic measurements by analyzing the intensity of emission features of highly ionized charge states, in particular those of iron. To properly interpret the emission, sophisticated models that rely heavily upon atomic physics rates and available databases of identified emission lines are necessary. Improvements in observational capabilities (e.g., higher spectral resolution) that resulted from the launch of the *Chandra X-ray Observatory* and the *X-ray Multi-Mirror Mission* (*XMM*) put more stringent demands on the quality of modeling calculations, especially those for the iron L-shell emission, which are prominent in many astrophysical sources.

Unfortunately, the comprehensiveness and accuracy of the present models is still lacking. This has been affirmed in the analysis of the Fe L-shell spectrum of Capella (Behar et al. 2001). The Hebrew University Lawrence Livermore Atomic Code (HULLAC) (Bar-Shalom et al. 2001) was used to model line emission from Fe xvi to Fe xviii. While the line intensities were quite well reproduced, the line positions more often than not did not match the observations. This does not cause problems where there are a few strong lines so that line assignments can be readily made.

However, it causes problems when there is a multitude of densely spaced lines each with similar intensities. These problems were resolved in the analysis of Capella by substituting wavelengths measured in the laboratory for the calculated wavelengths. The laboratory measurements employed in that study were done on the Lawrence Livermore National Laboratory (LLNL) electron beam ion trap EBIT-II (Brown et al. 1998, 2002) and included Fe xvii (Ne-like) to Fe xxiv (Li-like). Line identification and wavelength measurements of the $\Delta n \geq 1$ lines between 10 and 15 Å were determined by using plasmas with beam energies, $E_{\rm beam}$, of 1.15–4.6 keV and electron densities, n_e, $\approx 10^{12}$ cm^{-3}.

The need for line identifications and accurate wavelengths from lower charge states (Na-like and below) became clear in a subsequent study of the intensity ratios of the measurement of the 3C and 3D lines of Fe xvii (Ne-like) (Brown et al. 2001). It was found that Fe xvi lines blended with the 3D line, strongly enhancing its intensity, especially in low-temperature plasmas.

Creating X-ray line emission from charge states lower than Fe xvii is difficult in an electron beam ion trap. The reason is that the electron energy required to excite a given L-shell X-ray transition is almost twice that required to ionize the ion. There are no low-energy electrons in the monoenergetic beam that can lower the charge balance by either radiative electron recombination

TABLE 1
Summary of Laser Facilities and Plasma Conditions

Parameter	Tor Vergata University: Roma	Hercules: ENEA Frascati	COMET (LLNL)	
			Long Pulse	Short Pulse
Laser type.............................	Nd glass	XeCl	Nd-glass	Nd-glass
Laser wavelength	1054 nm	308 nm	1054 nm	1054 nm
Energy	1–6 J	0.5–1 J	5 J	5 J
Pulse duration	15 ns	12 ns	600 ps	1.0 ps
Spot size..	200 μm	50–70 μm	150 μm x 1.1 cm	80 μm x 1.1 cm
Intensity on target (W cm^{-2})............	$(0.2-1) \times 10^{12}$	10^{12}	10^{12}	5×10^{14}
T_e (eV)...	200–300	100–200	Bulk = 300–500	Bulk = 300–500
n_e (cm^{-3})......................................	$10^{20}-10^{21}$	$10^{21}-10^{22}$	$10^{20}-10^{22}$	$10^{20}-10^{22}$
Hot electrons......................................	No	No	$10^{-6}-10^{-3}$	$10^{-6}-10^{-3}$
Optically thick plasma........................	Yes	Smaller than Nd-glass ns laser $\approx$200 μm	Yes	Yes
Spectrometer resolving power	4000	4000	4000	4000

or by dielectronic recombination. The charge balance in an electron beam ion trap, therefore, tends to peak nearly exclusively at Fe XVII with little or no Fe XVI or Fe XV. By contrast, a plasma with a Maxwell-Boltzmann electron distribution has a sufficient number of low-energy electrons to produce lower charge states. Plasmas with low temperature, T_e, can thus provide information on dielectronic satellites that can blend with Fe XVII lines.

In this paper, we present X-ray spectra of iron that were recorded from laser-produced plasmas with electron temperatures between 100 and 500 eV and electron densities between 10^{20} and 10^{22} cm^{-3}. These densities are much higher than most astrophysical sources observed at high spectral resolution by *Chandra* and *XMM*, but the measurements aid the development of accurate atomic physics structure models and improved emission models. The plasma conditions produced bright emission for Fe XIV (O-like) lines all the way to Fe XV (Mg-like). Intensity-calibrated X-ray crystal spectrometers (Faenov et al. 1994; Pikuz et al. 1995; Skobelev et al. 1995; Young et al. 1998) recorded with a high spectral resolution, $(\lambda/\Delta\lambda)$, $\approx$4000, the $\Delta n \geq 1$ lines between 13.8 and 17.1 Å. The measured spectral resolution was less due to plasma broadening mechanisms. With this resolution much structure in the Na- and Mg-like satellites can be seen in proximity to the Ne-like 3C and 3D lines. Blending of the Ne-like iron lines with the Na- and Mg-like lines is evident. Approximately 80 emission lines of O- to Mg-like iron were identified through comparisons with calculations from HULLAC. HULLAC was used to calculate the atomic structure and rates. Accurate wavelength values were determined from the recorded spectra and compared with previous measurements and predictions from HULLAC. The majority of the HULLAC X-ray wavelengths differed by less than $\approx$20 mÅ from the measured wavelengths with a few differences above 50 mÅ. Our experimental wavelengths were on average less than 8 mÅ from the wavelengths measured by Brown et al. (1998, 2002).

HULLAC was used to generate simulated spectra for each ionization state for comparison with the experimental spectra recorded from plasmas created by the Hercules laser at the Ente per le Nuove Tecnologie, l'Energia e l'Ambiente (ENEA). The HULLAC spectra simulated the spectra fairly well when both dielectronic recombination (DR) and excitation autoionization (EA) processes and the optical depth effects for 200 μm of plasma were included. However, the level of agreement between the measured and the synthetic intensities varied for the different charge states. The Ne-, Na-, and Mg-like iron features were generally well modeled. Some of the stronger F-like line intensities were properly modeled by HULLAC. However, many of the F-like

lines recorded between 14 and 15 Å were much stronger in intensity than in the HULLAC model.

2. LASER FACILITIES

The X-ray spectra that we present in this paper were recorded from plasmas created at three different laser facilities: the Tor Vergata University (TVG) (Fournier et al. 2003a) laser in Rome (Italy), the Hercules laser (Bollanti et al. 1995, 1996; Lazzaro 1998) at ENEA in Frascati (Italy), and the Compact Multipulse Terawatt (COMET) laser (Dunn et al. 1999) at LLNL in Livermore, California (USA). The plasma and laser parameters from these three experiments are summarized in Table 1. In these plasmas we recorded the $\Delta n \geq 1$ emission lines of Fe XV (Mg-like) to Fe XIV (O-like) between 13.8 and 17.1 Å. Additionally, fluorine lines from Teflon[1] (C_2F_4)x plasmas were recorded at the Hercules laser facility for accurate wavelength calibrations of the spectrometers.

The first set of experiments were performed with the laser at TVG. The plasmas were created with a Quantel Nd:glass laser having a chain of two Nd:Yag and two Nd:Glass amplifiers. The laser pulses at the fundamental output wavelength of 1054 nm were 15 ns in duration in a Gaussian temporal profile. The repetition rate was limited to 1 shot per minute due to thermal lensing effects in the laser optics. A doublet lens with a 20 cm focal length focused the laser beam onto a spot of $\approx$200 μm in diameter at best focus and at an angle of incidence of 45° to the target material. The laser flux density was between 0.2 and 1 $\times$ 10^{12} W cm^{-2} with a maximum of 6 J in the pulse. The electron temperature of the plasma could be reduced by decreasing the laser energy and by defocusing the laser beam at the target. Moving the focusing optics out of best focus by 5 mm resulted in a laser spot size of $\approx$500 μm. At this lens position, the chosen laser energy was either 2 or 4 J in each pulse. By reducing the temperature, X-ray emission from O- and F-like iron ions was suppressed with respect to the emission from Na- and Mg-like ions (Fig. 1).

The second set of experiments was performed with the Hercules laser at ENEA. The ENEA facility had the optimal geometric orientation for the spectrometer to obtain accurate emission line wavelength measurements. Hercules is a XeCl excimer laser operated with an energy density slightly higher than the TVG laser. Each laser pulse contained 0.5–1 J in 12 ns at a wavelength of at 308 nm with a repetition rate of 0.5 Hz. The laser beam could be focused to a spot of 50–70 μm in diameter

---

[1] Registered Trademark of DuPont.
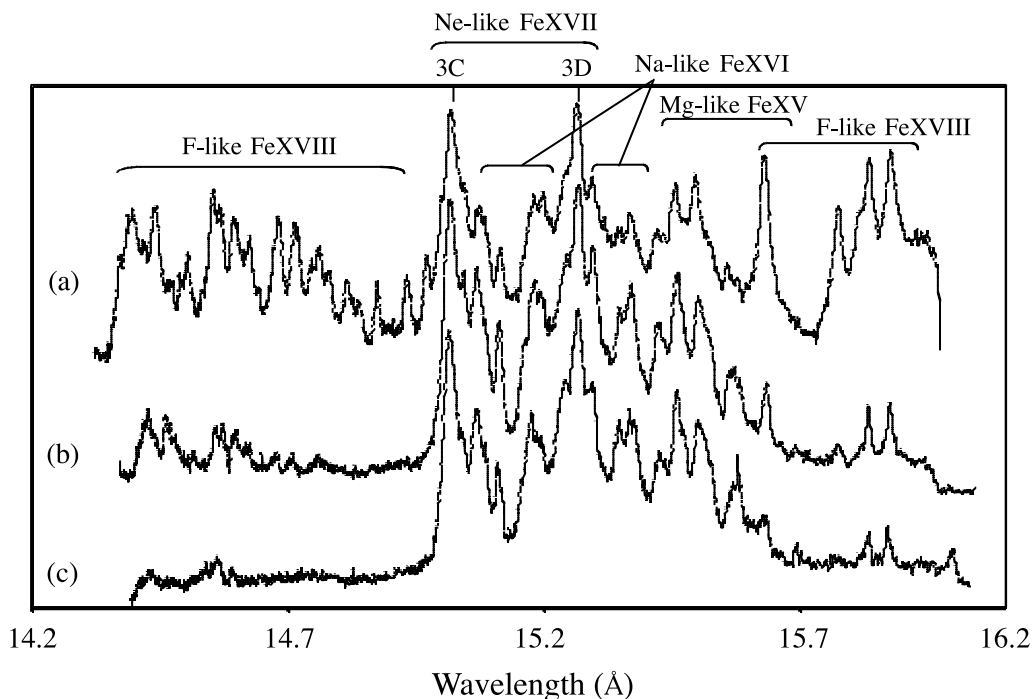
F_{IG}. 1.—Typical X-ray spectra of Fe between 14 and 16 Å obtained in plasmas produced by the 15 ns Nd:glass laser at Tor Vergata University: (*a*) laser pulse energy 6 J, laser spot 200 μm; (*b*) laser energy 4 J, laser spot 500 μm; (*c*) laser energy 2 J, laser spot 500 μm.

onto the Fe or Teflon targets. The resulting laser intensity on the target was about 10^{12} W cm^{-2}. These plasmas have been previously diagnosed to have $T_e \approx 200$ eV and $n_e \approx 10^{21}$ cm^{-3} by Vergunova et al. (1997) from K-shell spectra.

The third set of experiments was conducted at the Compact Multipulse Terawatt (COMET) laser at LLNL, which is the highest energy density laser of the three and is routinely used for X-ray laser experiments. The laser consists of a hybrid chirped pulse amplification system with a Ti:Sapphire oscillator and a regenerative four-stage Nd:phosphate glass amplifier at a wavelength of 1054 nm. The system has two separate beams that can deliver a maximum 7.5 J energy in a 500 fs short pulse (FWHM) and 15 J in a 600 ps long pulse (FWHM) to the target area. The laser repetition rate is 1 shot every 4 minutes. The short-pulse arm was created by compression in a vacuum grating compressor box. The short-pulse beam was sent through a delay line so that it arrived approximately 1.4 ns after the peak of the long-pulse beam. The two beams were co-aligned and propagated under vacuum to the target chamber and focused to a line 1.1 cm in length by using a cylindrical lens and an on-axis paraboloid. The long pulse was defocused to a width of $\approx$150 μm (FWHM), while the short-pulse beam was focused to $\approx$80 μm. Typically, 5 J of energy was delivered by each beam in the line focus giving a nominal intensity of 10^{12} W cm^{-2} in the long-pulse beam and 5×10^{14} W cm^{-2} in the short-pulse beam. These plasmas were the most complex both in the atomic and plasma physics since they were created by two different laser pulses of much different timescales.

3. SPECTROMETER AND TARGETS

Spatially resolved X-ray spectra of Fe xiv (O-like) to Fe xv (Mg-like) and F ix (H-like) and F viii (He-like) ions were recorded with two separate Focusing Spectrometers with Spatial Resolution (FSSR 2D) (Faenov et al. 1994; Pikuz et al. 1995; Skobelev et al. 1995; Young et al. 1998) in the 13.8–17.1 Å spectral range. One spectrometer had a large 15×50 mm^2

spherically bent mica crystal with a 150 mm radius of curvature. The second had a small spherically bent 10×30 mm^2 mica crystal with a 100 mm radius of curvature. Both mica crystals had a lattice spacing $2d = 19.915$ Å using the 002 lattice plane. Covering the wavelength range with two different crystals allowed a much higher instrumental spectral resolution ($\lambda/\Delta\lambda \approx$ 4000) than would be possible with a single crystal. The effective spectral resolution for the spectrometers varied from 1000 to 4000 and was limited mainly by the Doppler broadening of the spectral lines from the plasma expansion. The high spectral resolution limited the wavelength coverage to only 1.3–2.6 Å at a given position. Overlapping spectral ranges were recorded to cover the entire region adequately. The spatial resolution of the spectrometers varied from 20 to 50 μm.

To measure the $3p \rightarrow 2s$ and the $3d \rightarrow 2p$ resonance lines of Ne-like iron, the 150 mm radius of curvature crystal was positioned to put the wavelength of 14.7 Å at the film center with a Bragg angle of $\approx$47°.6. The distance from the target to the crystal was 30 cm. The distance from the crystal to the detector plane was 15.36 cm. This configuration had a spectral coverage of $\approx$2 Å.

Spectra were recorded on KODAK RAR 2492 or RAR 2497 X-ray film. The procedure developed by Henke et al. (1984) was adopted for developing, scanning with a microdensitometer and converting the film density to incident X-ray photon intensity. The film holder was protected by two 1 μm thick polypropylene filters coated with 0.2 μm of aluminum on both sides. Additionally, a 2 μm polypropylene filter was used to protect the crystal from plasma debris. The intensities of the lines were corrected for the filter transmissions. The crystal reflectivities were assumed to vary slowly over this spectral range and were not included in the calibrations.

Stepped targets were used in the Hercules experiments (see Fig. 2). A sample experimental configuration and spectra are shown in Figure 2. The targets were made of Teflon cut into the shape of a step. The step heights varied between 300 and 800 μm. A 60 μm thick 99.9% pure iron foil was glued to the surface of
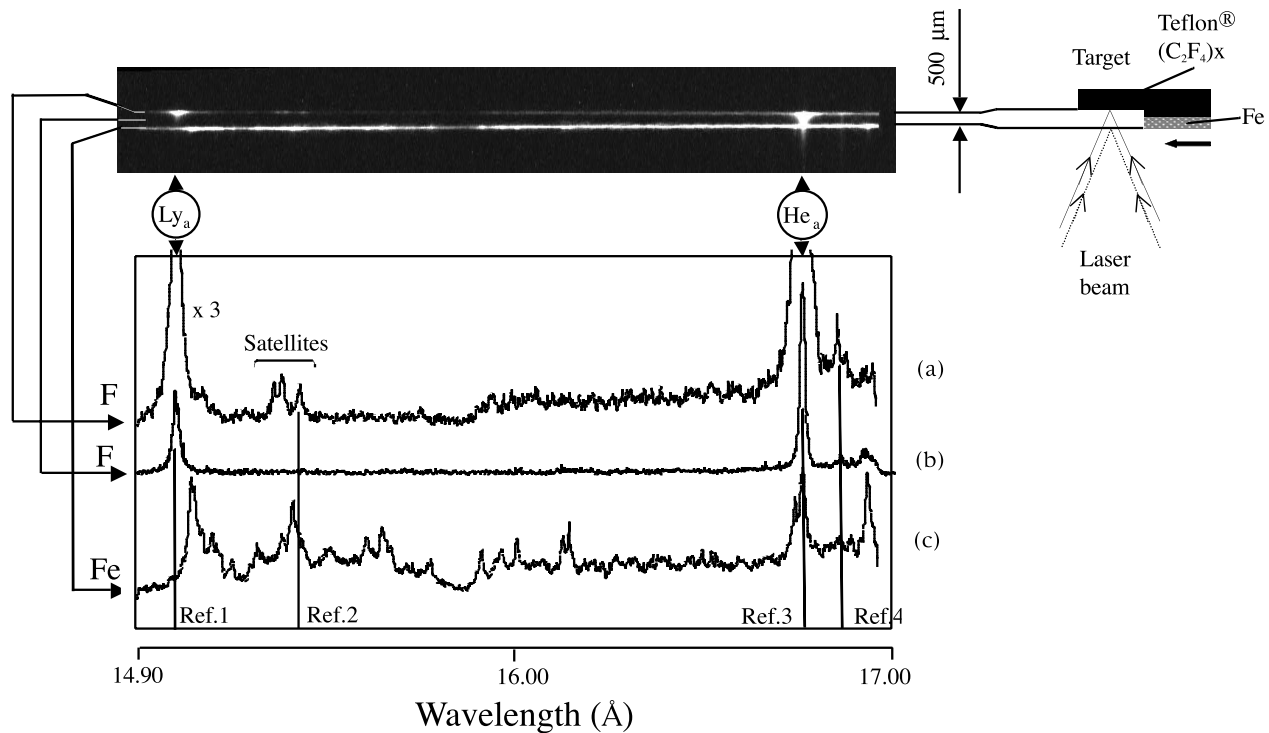
FIG. 2.—Space-resolved images in the direction of plasma expansion of F K-shell and Fe L-shell X-ray line emission, obtained at Hercules. The step between Teflon and Fe targets was 500 μm. Traces of Lyα and its satellite, as well as the resonance and intercombination lines of F VIII, which were used as a reference lines, are marked. The upper and middle traces of fluorine were done at different distances from the surface of the target along the spatial direction of the image. The bottom trace showing the Fe emission was obtained when Fe was irradiated by a laser intensity of 10^{12} W cm^{-2}. Reference 1 is the $2p$ ($^2P_{3/2}$) $\rightarrow$ $1s$ ($^2S_{1/2}$) of F IX at 14.9823 Å. Reference 2 is the $2p^2$ ($^1D_2$) $\rightarrow$ $1s2p$ ($^2P_1$) of F VIII at 15.2910 Å. Reference 3 is the $1s2p$ ($^1P_1$) $\rightarrow$ $1s^2$ ($^1S_0$) of F VIII at 16.8068 Å. Reference 4 is the $1s2p$ ($^3P_1$) $\rightarrow$ $1s^2$ ($^1S_0$) of F VIII at 16.9499 Å.

the higher Teflon step. The Fe and Teflon targets were translated into the beam of the laser on different shots to obtain both an iron and fluorine spectrum on the same film. The Teflon plasma produced the H-like and He-like F spectral lines that were used for the wavelength calibration of the spectrometers. The step on each target physically separated the two spectral images on the film and slightly changed the geometry and dispersion curve of the spectrometers. The variation in the dispersion curve was investigated by recording spectra for targets with different Teflon step heights. For the COMET and TVG experiments the targets consisted of flat 1 mm thick, polished slabs of Fe.

To obtain sufficiently bright images on the film, multiple shots at each experimental condition were required. The number of shots at a given condition was different at each of the laser facilities. The spectral images were obtained in 1–10 shots with the TVG laser, 50–100 shots with the Hercules laser, and 3–10 shots with the COMET laser. The laser conditions were kept constant for each spectral image with the laser energy varying less than ±5% from shot to shot.

4. WAVELENGTH CALIBRATIONS

Accurate wavelength measurements of ≈80 O- to Mg-like iron were determined in the 13.8–17.1 Å spectral range from the spectra recorded at the ENEA laser facility. The large vacuum chamber that was available at ENEA allowed the spectrometers to be placed with an optimal view of the expanding plasma. The spectrometers recorded the X-ray spectra perpendicular to the ions' motion after their acceleration from the targets surface due to laser heating. With this view, the effect of the Doppler shift of the moving ions on the wavelength of the X-ray lines was minimized.

The spectrometer dispersion curves were calculated by using the Multicharged Ions Spectra Data Center (MISDC) of the National Research Institute for Physical-Technical and Radio-technical Measurement's (VNIIFTRI) ray-tracing code specially created for the FSSR spectrometers (Magunov et al. 1995). The dispersion curves are calculated ab initio through deterministic ray tracing of the X-rays assuming equations of geometrical optics and the Bragg reflection law for the crystals. The calculations included the geometry of the experimental setup at each laser facility (e.g., the relative distances between the crystal, film and plasma). The reliability of the calculations depended on the accurate determination of these parameters. Unfortunately, some of these distances are not well known in our experiments. With these uncertainties, the resulting dispersion curves would introduce at least a 10 mÅ error in the absolute wavelength measurements. This uncertainty can be reduced by using the calculated ab initio dispersion curves in combination with at least three well-known calibration lines.

The dispersion curves are best approximated by a cubic polynomial:

$$\lambda = a + bX + cX^2 + dX^3 \quad (1).$$

The variables a, b, c, and d are coefficients determined through fits that include both the results of the calculations and the measured positions of the calibration lines. The variables X and λ are the position in cm on the film and the resulting wavelength in Å. This form was chosen since it was the lowest-order polynomial with acceptable accuracy. The second-order polynomial had an error of ≈4 mÅ, which was too large for our measurements.

TABLE 2
CALIBRATION LINES AND REFERENCE WAVELENGTH VALUES

Transition	Ion	λ(Å)
$2p\ (^2P_{3/2}) \rightarrow 1s\ (^2S_{1/2})$	F IX	14.9823
$2p\ (^2P_{1/2}) \rightarrow 1s\ (^2S_{1/2})$	F IX	14.9877
$1s4p\ (^1P_1) \rightarrow 1s^2\ (^1S_0)$	F VIII	13.7815
$1s3p\ (^1P_1) \rightarrow 1s^2\ (^1S_0)$	F VIII	14.4580
$1s2p\ (^1P_1) \rightarrow 1s^2\ (^1S_0)$	F VIII	16.8068
$1s2p\ (^3P_1) \rightarrow 1s^2\ (^1S_0)$	F VIII	16.9499
$2p^2\ (^1D_2) \rightarrow 1s2p\ (^2P_1)$......................	F VIII	15.2910
$2p_{1/2}2p^4_{3/2}3d_{3/2} \rightarrow 2p^6$	Fe XVII	15.014 ± 0.001

The third-order polynomial diverged from the calculated dispersion curve by at most 0.3 mÅ. By using the known calibration lines, calculations of the dispersion curves for various relative positions of the plasma, crystal and film, the error in the dispersion curve was reduced to several tenths of a mÅ.

The well-known transitions in H- and He-like fluorine (Boiko et al. 1994; Drake 1988; Garcia & Mack 1963) were used as calibration lines (see Table 2). These lines have been calculated with much higher accuracy than the uncertainty in our measurements. The lines used were the $2p \rightarrow 1s$ Ly$\alpha_{1,2}$ transitions in H-like and the $1snp \rightarrow 1s^2\ (^1P_1 \rightarrow {}^1S_0)$ and $1snp \rightarrow 1s^2\ (^3P_1 \rightarrow {}^1S_0)$ in He-like ($n = 2$, 3, or 4). Additionally, the $2p^2 \rightarrow 1s2p$ ($^1D_2 \rightarrow {}^2P_1$) transition in F VIII was used at 15.2910 Å (Brunetkin et al. 1992). For the 13.7–15.1 Å spectral region, the 3C-line of Ne-like Fe measured in the other spectral range (with an accuracy 1.0 mÅ) was used as an additional reference line (Brown et al.

1998) along with the Heγ $1s3p \rightarrow 1s^2$ ($^1P_1 \rightarrow {}^1S_0$), He$\beta$ $1s4p \rightarrow 1s^2$ ($^1P_1 \rightarrow {}^1S_0$) and Ly$\alpha_{1,2}$ transitions. Since He β and He γ are spectrally broader and weaker than Lyα, the measurement uncertainty was larger below 14.5 Å.

The relative location in cm of each of the iron and fluorine lines on the film was determined by two different methods. In the first method, the position of each line, X_{max}, at its peak intensity was determined. In the second method, the profile of each Fe line was fitted with a Gaussian function to determine the position of its centroid, X_{cent}, and its intensity. For most cases difference ($X_{max} - X_{cent}$) was very small. In a few cases the difference of $X_{max} - X_{cent}$ was significant and was included in the measurement error. The wavelength was determined from ($X_{max} + X_{cent}$)/2. The uncertainty in the determination of the centroid wavelength of each line was ≈ 0.2 mÅ.

The iron and Teflon samples were at slightly different distances from the spectrometer in the experiment due to the step nature of the target. The difference in the dispersion in the spectrometer due to the different target positions was investigated. Spectra were taken of the same emission lines with various step heights and resulting positions on the film. The differences in the line positions and dispersion were found to be small. The smallest shift occurred when the spectrometer's view was normal to the plasma expansion or perpendicular to the normal of the incident laser beam. With this view, the largest change in the line positions was ≈ 0.2 mÅ. The spectrometers were in this orientation at ENEA. Additionally, the fluorine images overlapped the iron spectral images as seen in traces a, b, and c of Figure 2. The fluorine calibration lines appeared on the same lineouts as the iron lines.

TABLE 3
PREDICTED AND IDENTIFIED BRIGHT LINES OF Fe XV (Mg-LIKE)

Label	λ_{exp} (Å)	λ_{HUL} (Å)	I_{ENEA}	I_{HUL} (A)	I_{HUL} (B)	I_{HUL} (C)	$J_{upper} \rightarrow J_{lower}$	Configuration
Mg1	15.583 (3)	15.5888	0.14	0.08	0.40	0.53	$3 \rightarrow 2$	$2s^22p_{1/2}2p^3_{3/2}3p^3_{3/2}3d^2_{5/2} \rightarrow 2s^22p^63p_{1/2}3d_{3/2}$
Mg2	15.523 (1)	15.5397	1.00	0.14	0.45	0.59	$4 \rightarrow 3$	$2s^22p_{1/2}2p^3_{3/2}3s3d^2_{5/2} \rightarrow 2s^22p^63s3d_{5/2}$
...	...	15.5074	...	0.34	0.42	0.56	$3 \rightarrow 2$	$2s^22p_{1/2}2p^4_{3/2}3s3p_{1/2}3d_{5/2} \rightarrow 2s^22p^63s3p_{3/2}$
...	...	15.4605	...	0.23	0.59	0.70	$3 \rightarrow 2$	$2s^22p_{1/2}2p^4_{3/2}3s3d^2_{5/2} \rightarrow 2s^22p^63p_{1/2}3p_{3/2}$
Mg3	15.475 (1)	15.4749	1.00	0.42	0.56	0.69	$2 \rightarrow 1$	$2s^22p_{1/2}2p^3_{3/2}3s3p_{3/2}3d_{3/2} \rightarrow 2s^22p^63s3p_{1/2}$
...	...	15.4492	...	0.23	0.42	0.55	$2 \rightarrow 2$	$2s^22p_{1/2}2p^4_{3/2}3p_{1/2}3d_{5/2} \rightarrow 2s^22p^63p_{1/2}3d_{5/2}$
...	...	15.4426	...	0.37	0.42	0.56	$1 \rightarrow 0$	$2s^22p_{1/2}2p^4_{3/2}3s3p_{1/2}3d_{3/2} \rightarrow 2s^22p^63s3p_{1/2}$
...	...	15.4334	...	0.60	0.79	0.88	$4 \rightarrow 4$	$2s^22p_{1/2}2p^4_{3/2}3p_{3/2}3d_{3/2}3d_{5/2} \rightarrow 2s^22p^63p_{3/2}3d_{5/2}$
Mg4b..............	15.460 (1)	15.4234	0.80	0.83	0.82	0.91	$2 \rightarrow 2$	$2s^22p_{1/2}2p^3_{3/2}3s3p_{3/2}3d_{3/2} \rightarrow 2s^22p^63s3p_{3/2}$
...	...	15.4067	...	0.26	0.45	0.59	$3 \rightarrow 3$	$2s^22p_{1/2}2p^4_{3/2}3p_{3/2}3d_{3/2}3d_{5/2} \rightarrow 2s^22p^63p_{1/2}3d_{5/2}$
Mg5	15.426 (3)	15.3998	0.13	0.80	0.78	0.89	$1 \rightarrow 2$	$2s^22p_{1/2}2p^4_{3/2}3s3p_{3/2}3d_{3/2} \rightarrow 2s^22p^63s3p_{3/2}$
...	...	15.3987	...	0.59	0.61	0.73	$2 \rightarrow 3$	$2s^22p_{1/2}2p^4_{3/2}3p_{3/2}3d_{3/2}3d_{5/2} \rightarrow 2s^22p^63p_{3/2}3d_{5/2}$
...	...	15.3813	...	0.12	0.69	0.78	$5 \rightarrow 4$	$2s^22p_{1/2}2p^4_{3/2}3p_{3/2}3d_{3/2}3d_{5/2} \rightarrow 2s^22p^63p_{3/2}3d_{5/2}$
...	...	15.3773	...	0.27	0.55	0.68	$3 \rightarrow 2$	$2s^22p_{1/2}2p^4_{3/2}3s3p_{3/2}3d_{5/2} \rightarrow 2s^22p^63s3p_{3/2}$
...	...	15.3744	...	0.64	1.00	1.00	$3 \rightarrow 3$	$2s^22p_{1/2}2p^4_{3/2}3p_{3/2}3d^2_{3/2} \rightarrow 2s^22p^63p_{3/2}3d_{3/2}$
...	...	15.3721	...	0.32	0.40	0.54	$3 \rightarrow 4$	$2s^22p_{1/2}2p^3_{3/2}3p_{1/2}3d_{3/2}3d_{5/2} \rightarrow 2s^22p^63p_{3/2}3d_{5/2}$
Mg6	15.372 (1)	15.3702	0.81	0.95	0.73	0.86	$1 \rightarrow 1$	$2s^22p_{1/2}2p^4_{3/2}3s3p_{3/2}3d_{3/2} \rightarrow 2s^22p^63s3p_{3/2}$
Mg7	15.367 (1)	15.3670	0.85	0.29	0.71	0.79	$2 \rightarrow 1$	$2s^22p_{1/2}2p^4_{3/2}3s3p_{3/2}3d_{3/2} \rightarrow 2s^22p^63s3p_{3/2}$
Mg8b..............	15.360 (2)	15.3744	0.37	0.64	1.00	1.00	$3 \rightarrow 3$	$2s^22p_{1/2}2p^4_{3/2}3p_{3/2}3d^2_{3/2} \rightarrow 2s^22p^63p_{3/2}3d_{3/2}$
...	...	15.3578	...	0.35	0.58	0.71	$3 \rightarrow 3$	$2s^22p_{1/2}2p^3_{3/2}3p_{1/2}3p_{3/2}3d_{3/2} \rightarrow 2s^22p^63s3d_{5/2}$
...	...	15.3411	...	0.10	0.49	0.62	$4 \rightarrow 3$	$2s^22p_{1/2}2p^4_{3/2}3s3d_{3/2}3d_{5/2} \rightarrow 2s^22p^63s3d_{5/2}$
Mg9	15.348 (2)	15.3323	0.34	0.63	0.75	0.81	$1 \rightarrow 0$	$2s^22p_{1/2}2p^3_{3/2}3s^23d_{3/2} \rightarrow 2s^22p^63s^2$
...	...	15.3250	...	1.00	0.73	0.87	$2 \rightarrow 2$	$2s^22p_{1/2}2p^3_{3/2}3s3d_{3/2}3d_{5/2} \rightarrow 2s^22p^63s3d_{5/2}$
...	...	15.3110	...	0.16	0.43	0.56	$2 \rightarrow 3$	$2s^22p_{1/2}2p^4_{3/2}3p_{3/2}3d^2_{3/2} \rightarrow 2s^22p^63p_{3/2}3d_{3/2}$
...	...	15.1354	...	0.40	0.41	0.60	$3 \rightarrow 2$	$2s^22p_{1/2}2p^4_{3/2}3s3d_{3/2}4p_{3/2} \rightarrow 2s^22p^63s4p_{3/2}$
...	...	15.1305	...	0.24	0.41	0.59	$4 \rightarrow 3$	$2s^22p_{1/2}2p^4_{3/2}3s3d_{3/2}4d_{5/2} \rightarrow 2s^22p^63s4d_{5/2}$
Mg10..............	15.113 (3)	15.0915	0.87	0.61	0.41	0.63	$5 \rightarrow 4$	$2s^22p_{1/2}2p^4_{3/2}3s3d_{3/2}5f_{7/2} \rightarrow 2s^22p^63s5f_{7/2}$
...	...	15.0833	...	0.87	0.51	0.76	$6 \rightarrow 5$	$2s^22p_{1/2}2p^4_{3/2}3s3d_{3/2}5g_{9/2} \rightarrow 2s^22p^63s5g_{9/2}$

NOTES.—A "b" after the label indicates a blend. "A"—Model A: optically thin. "B"—Model B: optically thin and EA/DR. "C"—Model C: optically thick and EA/DR. Models conditions were $n_e = 10^{21}$ cm^{-3} and $T_e = 200$ eV.

TABLE 4
PREDICTED AND IDENTIFIED BRIGHT LINES OF Fe XVI (Na-LIKE)

Label	λ_{exp} (Å)	λ_{HUL} (Å)	I_{ENEA}	I_{HUL} (A)	I_{HUL} (B)	I_{HUL} (C)	$J_{upper} \rightarrow J_{lower}$	Configuration
Na1b	15.500 (2)	15.4562	0.34	0.24	0.21	0.39	$\frac{3}{2} \rightarrow \frac{3}{2}$	$2s^22p_{1/2}2p_{3/2}^43p_{1/2}3d_{5/2} \rightarrow 2s^22p^63p_{3/2}$
Na2b	15.360 (2)	15.3534	0.28	0.47	0.51	0.53	$\frac{5}{2} \rightarrow \frac{3}{2}$	$2s^22p_{1/2}2p_{3/2}^43d_{3/2}^2 \rightarrow 2s^22p^63d_{3/2}$
Na3	15.304 (1)	15.2899	0.56	0.69	0.70	0.62	$\frac{5}{2} \rightarrow \frac{3}{2}$	$2s^22p_{1/2}^22p_{3/2}^33p_{3/2}3d_{5/2} \rightarrow 2s^22p^63p_{3/2}$
Na4	15.290 (1)	15.2687	0.95	0.75	0.77	0.69	$\frac{3}{2} \rightarrow \frac{1}{2}$	$2s^22p_{1/2}2p_{3/2}^43s3d_{5/2} \rightarrow 2s^22p^63s$
Na5	15.276 (1)	15.2552	0.59	0.75	0.90	0.64	$\frac{3}{2} \rightarrow \frac{1}{2}$	$2s^22p_{1/2}2p_{3/2}^43p_{1/2}3d_{3/2} \rightarrow 2s^22p^63p_{1/2}$
	. . .	15.2427	. . .	0.69	0.64	0.82	$\frac{3}{2} \rightarrow \frac{3}{2}$	$2s^22p_{1/2}2p_{3/2}^43p_{3/2}3d_{3/2} \rightarrow 2s^22p^63p_{3/2}$
Na6	15.237 (1)	15.2247	1.00	1.00	1.00	1.00	$\frac{5}{2} \rightarrow \frac{5}{2}$	$2s^22p_{1/2}2p_{3/2}^43d_{3/2}3d_{5/2} \rightarrow 2s^22p^63d_{5/2}$
Na7	15.213 (2)	15.2364	0.73	0.88	0.96	0.63	$\frac{7}{2} \rightarrow \frac{5}{2}$	$2s^22p_{1/2}2p_{3/2}^43d_{3/2}3d_{5/2} \rightarrow 2s^22p^63d_{5/2}$
Na8	15.174 (2)	15.2081	0.81	0.55	0.52	0.71	$\frac{1}{2} \rightarrow \frac{1}{2}$	$2s^22p_{1/2}2p_{3/2}^43s3d_{3/2} \rightarrow 2s^22p^63s$
	. . .	15.2000	. . .	0.44	0.42	0.67	$\frac{3}{2} \rightarrow \frac{3}{2}$	$2s^22p_{1/2}2p_{3/2}^43d_{3/2}^2 \rightarrow 2s^22p^63d_{3/2}$
Na9	15.159 (1)	15.1601	0.56	0.77	0.70	0.80	$\frac{5}{2} \rightarrow \frac{3}{2}$	$2s^22p_{1/2}2p_{3/2}^43p_{3/2}3d_{3/2} \rightarrow 2s^22p^63p_{3/2}$
Na10	15.087 (1)	15.0996	0.73	0.63	0.50	0.54	$\frac{3}{2} \rightarrow \frac{1}{2}$	$2s^22p_{1/2}2p_{3/2}^43p_{1/2}3p_{3/2} \rightarrow 2s^22p^63s$
Na11	15.064 (3)	15.0768	0.93	0.20	0.42	0.54	$\frac{7}{2} \rightarrow \frac{5}{2}$	$2s^22p_{1/2}2p_{3/2}^43d_{3/2}4d_{5/2} \rightarrow 2s^22p^64d_{5/2}$
Na12	15.031 (1)	15.0743	0.92	0.24	0.51	0.61	$\frac{7}{2} \rightarrow \frac{5}{2}$	$2s^22p_{1/2}2p_{3/2}^43d_{3/2}4f_{5/2} \rightarrow 2s^22p^64f_{5/2}$
	. . .	15.0081	. . .	0.22	0.43	0.55	$\frac{9}{2} \rightarrow \frac{7}{2}$	$2s^22p_{1/2}2p_{3/2}^43d_{3/2}4f_{7/2} \rightarrow 2s^22p^64f_{7/2}$
Na13b	14.097 (1)	14.0893	0.23	0.08	0.07	0.16	$\frac{5}{2} \rightarrow \frac{3}{2}$	$2s2p^63p_{1/2}3p_{3/2} \rightarrow 2s^22p^63p_{3/2}$
Na14b	14.093 (1)	14.0866	0.23	0.12	0.10	0.22	$\frac{5}{2} \rightarrow \frac{3}{2}$	$2s2p^63p_{1/2}3d_{5/2} \rightarrow 2s^22p^63d_{3/2}$
Na15	14.060 (1)	14.0688	0.14	0.20	0.17	0.32	$\frac{7}{2} \rightarrow \frac{5}{2}$	$2s2p^63p_{3/2}3d_{5/2} \rightarrow 2s^22p^63d_{5/2}$
Na16	14.018 (3)	14.0161	0.25	0.07	0.06	0.13	$\frac{1}{2} \rightarrow \frac{1}{2}$	$2s2p^63s3p_{1/2} \rightarrow 2s^22p^63s$
Na17	13.938 (3)	13.9979	0.24	0.15	0.13	0.25	$\frac{3}{2} \rightarrow \frac{3}{2}$	$2s2p^63p_{3/2} \rightarrow 2s^22p^63p_{3/2}$

NOTES.—A "b" after the label indicates a blend. "A"—Model A: optically thin. "B"—Model B: optically thin and EA/DR. "C"—Model C: optically thick and EA/DR. Models conditions were $n_e = 10^{21}$ cm^{-3} and $T_e = 200$ eV.

The total error on each measured wavelength included the accuracy in determining the dispersion curve, the accuracy of the calibration lines and the uncertainty in determining the centroid of the fluorine calibration and the iron lines. The total uncertainty in a given wavelength measurement was usually 1–2 mÅ. Although, some uncertainties were as large as 6 mÅ. The wavelengths for each transition determined from the ENEA spectra are listed in Tables 3, 4, 5, 6, and 7 for O-like to Mg-like iron, respectively, with the uncertainties in mÅ given in parenthesis after each wavelength.

5. MODELING OF WAVELENGTHS AND LINE INTENSITIES

The HULLAC atomic data package was used to calculate the atomic structure, transition rates, and wavelengths for O-like to Mg-like iron ions. Synthetic spectra were produced for comparisons with the recorded spectra from the different laser experiments.

The radiative transition rates and energy level structure of each ionization state were calculated from the Dirac equa-

tion with a parametric potential. Electron impact excitation cross sections, σ, were calculated semirelativistically in the distorted wave approximation. The electron-impact excitation rate coefficients, $Q = \langle \sigma v \rangle$, were obtained by integrating over a Maxwell-Boltzmann electron energy distribution. The variable, v, is the velocity of the electrons.

The number of levels used in the modeling for each isoelectronic sequence varied. In general the levels included $n = 3$, 4, or 5 and $l = s, p, d, f$, or g. Many excited levels were included of the form $2s^22p^knl$ and $2s2p^{k+1}nl$ with $n = 3$, 4, or 5 and $l = s, p, d, f$, or g. A detailed list of the levels included for each ion is shown in Table 8.

Synthetic spectra were calculated for three different conditions: model A was an optically thin plasma with no contributions of EA/DR to the line intensities, model B was an optically thin plasma that included EA/DR contributions to the line intensities, and model C was an optically thick plasma that included EA/DR contributions to the line intensities. For model A, the level populations for each ionization state were not coupled

TABLE 5
PREDICTED AND IDENTIFIED BRIGHT LINES OF Fe XVII (Ne-LIKE)

Label	λ_{exp} (Å)	λ_{HUL} (Å)	λ_{FAC} (Å)	$\|\lambda_{HUL} - \lambda_{FAC}\|$ (Å)	λ_{Brown}[a] (Å)	$\lambda_{Phillips}$[b] (Å)	I_{ENEA}	I_{HUL} (A)	I_{HUL} (B)	I_{HUL} (C)	$J_{upper} \rightarrow J_{lower}$	Configuration
3G	17.036 (1)	17.0706	17.0824	0.0118	17.051 (1)	17.055	0.76	0.13	0.13	0.78	$1 \rightarrow 0$	$2s^22p_{1/2}^22p_{3/2}^33s \rightarrow 2s^22p^6$
3F	16.778 (1)	16.7930	16.8075	0.0145	16.780 (2)	16.780	0.65	0.11	0.11	0.75	$1 \rightarrow 0$	$2s^22p_{1/2}2p_{3/2}^43s \rightarrow 2s^22p^6$
3Eb	15.460 (1)	15.4706	15.4829	0.0123	15.453 (5)	15.456	0.38	0.01	0.01	0.34	$1 \rightarrow 0$	$2s^22p_{1/2}^22p_{3/2}^33d_{3/2} \rightarrow 2s^22p^6$
3Db	15.267 (1)	15.2708	15.2839	0.0131	15.261 (2)	15.265	0.85	0.38	0.38	0.85	$1 \rightarrow 0$	$2s^22p_{1/2}^22p_{3/2}^33d_{5/2} \rightarrow 2s^22p^6$
3Cb	15.014 (1)	15.0087	15.0253	0.0166	15.014 (1)	15.012	1.00	1.00	1.00	1.00	$1 \rightarrow 0$	$2s^22p_{1/2}2p_{3/2}^43d_{3/2} \rightarrow 2s^22p^6$
3B	13.891 (1)	13.8646	13.8675	0.0029	13.892 (3)	13.890	0.19	0.02	0.02	0.43	$1 \rightarrow 0$	$2s2p^63p_{1/2} \rightarrow 2s^22p^6$
3A	13.828 (1)	13.7971	13.8001	0.0030	13.825 (2)	13.824	0.50	0.16	0.16	0.63	$1 \rightarrow 0$	$2s2p^63p_{3/2} \rightarrow 2s^22p^6$
4C	. . .	12.1324	12.1422	0.0098	12.124 (1)	12.122	. . .	0.10	0.10	0.38	$1 \rightarrow 0$	$2s^22p_{1/2}2p_{3/2}^44d_{3/2} \rightarrow 2s^22p^6$

NOTES.—A "b" after the label indicates a blend. "A"—Model A: optically thin. "B"—Model B: optically thin and EA/DR. "C"—Model C: optically thick and EA/DR. Models conditions were $n_e = 10^{21}$ cm^{-3} and $T_e = 200$ eV.
[a] Brown et al. (1998).
[b] Phillips et al. (1999, 1982).

TABLE 6
PREDICTED AND IDENTIFIED BRIGHT LINES OF Fe XVIII (F-LIKE)

Label	λ_{exp} (Å)	λ_{HUL} (Å)	λ_{FAC} (Å)	$|\lambda_{\text{HUL}} - \lambda_{\text{FAC}}|$ (Å)	λ_{Brown}[a] (Å)	$\lambda_{\text{Phillips}}$[b] (Å)	I_{ENEA}	I_{HUL} (A)	I_{HUL} (B)	I_{HUL} (C)	$J_{\text{upper}} \to J_{\text{lower}}$	Configuration
F2	. . .	16.3223	16.3313	0.0090	16.320 (5)	16.310	0.00	0.02	0.02	0.02	$\frac{3}{2} \to \frac{1}{2}$	$2s2p_{1/2}^2 2p_{3/2}^3 3s \to 2s2p^6$
F3	16.164 (3)	16.1730	16.1809	0.0079	16.159 (5)	16.170	0.10	0.05	0.05	0.05	$\frac{3}{2} \to \frac{1}{2}$	$2s2p_{1/2}2p_{3/2}^4 3s \to 2s2p^6$
F4	16.069 (3)	16.0878	16.0970	0.0092	16.071 (3)	16.074	0.10	0.01	0.01	0.01	$\frac{5}{2} \to \frac{3}{2}$	$2s^2 2p_{1/2}^2 2p_{3/2}^2 3s \to 2s^2 2p_{1/2}^2 2p_{3/2}^3$
F5	16.038 (2)	16.0284	16.0335	0.0051	16.045 (10)	16.020	0.28	0.05	0.05	0.06	$\frac{1}{2} \to \frac{1}{2}$	$2s^2 2p_{1/2} 2p_{3/2}^3 3s \to 2s^2 2p_{1/2} 2p_{3/2}^4$
F6	16.019 (2)	16.0130	16.0207	0.0077	16.004 (2)	. . .	0.39	0.16	0.16	0.18	$\frac{3}{2} \to \frac{3}{2}$	$2s^2 2p_{1/2}^2 2p_{3/2}^2 3s \to 2s^2 2p_{1/2}^2 2p_{3/2}^3$
F7	15.934 (5)	15.8802	15.8869	0.0067	15.931 (8)	. . .	0.04	0.00	0.00	0.00	$\frac{1}{2} \to \frac{3}{2}$	$2s^2 2p_{1/2}^2 2p_{3/2}^2 3s \to 2s^2 2p_{1/2}^2 2p_{3/2}^3$
F8	15.881 (2)	15.8770	15.8879	0.0109	15.870 (3)	15.868	0.34	0.10	0.10	0.12	$\frac{3}{2} \to \frac{1}{2}$	$2s2p_{1/2}2p_{3/2}^4 3s \to 2s^2 2p_{1/2}^2 2p_{3/2}^3$
F9	15.832 (2)	15.8418	15.8485	0.0067	15.824 (3)	15.828	0.30	0.09	0.09	0.10	$\frac{3}{2} \to \frac{3}{2}$	$2s^2 2p_{1/2} 2p_{3/2}^3 3s \to 2s^2 2p_{1/2}^2 2p_{3/2}^3$
F10	15.778 (2)	15.7699	15.7755	0.0056	15.759 (5)	15.769	0.22	0.05	0.05	0.06	$\frac{1}{2} \to \frac{3}{2}$	$2s^2 2p_{1/2}^2 2p_{3/2}^2 3s \to 2s^2 2p_{1/2}^2 2p_{3/2}^3$
F11	15.627 (2)	15.6334	15.6449	0.0115	15.625 (3)	15.628	0.39	0.14	0.14	0.16	$\frac{5}{2} \to \frac{3}{2}$	$2s^2 2p_{1/2} 2p_{3/2}^3 3s \to 2s^2 2p_{1/2}^2 2p_{3/2}^3$
F12b	15.500 (2)	15.4440	15.4515	0.0075	15.494 (10)	15.498	0.35	0.03	0.03	0.04	$\frac{1}{2} \to \frac{1}{2}$	$2s^2 2p_{3/2}^4 3s \to 2s^2 2p_{1/2} 2p_{3/2}^4$
F12.1	14.974 (2)	14.9175	14.9254	0.0079	. . .	. . .	0.20	0.00	0.00	0.00	$\frac{3}{2} \to \frac{1}{2}$	$2s2p_{1/2}^2 2p_{3/2}^3 3d_{3/2} \to 2s^2 2p_{1/2} 2p_{3/2}^4$
F12.2	14.874 (2)	14.8882	14.8973	0.0091	. . .	. . .	0.18	0.02	0.02	0.02	$\frac{3}{2} \to \frac{1}{2}$	$2s^2 2p_{1/2}^2 2p_{3/2}^3 4s \to 2s2p^6$
F12.3	14.807 (2)	14.8227	14.8319	0.0092	. . .	. . .	0.17	0.03	0.03	0.03	$\frac{1}{2} \to \frac{1}{2}$	$2s2p_{1/2}^2 2p_{3/2}^3 3d_{3/2} \to 2s2p^6$
F12.4	14.775 (1)	14.7778	14.7852	0.0074	. . .	. . .	0.13	0.02	0.02	0.02	$\frac{3}{2} \to \frac{1}{2}$	$2s^2 2p_{1/2}^2 2p_{3/2}^3 3d_{5/2} \to 2s^2 2p_{1/2} 2p_{3/2}^4$
F12.5	14.758 (1)	14.7631	14.7730	0.0099	. . .	. . .	0.22	0.08	0.08	0.09	$\frac{3}{2} \to \frac{1}{2}$	$2s2p_{1/2}2p_{3/2}^4 3d_{5/2} \to 2s2p^6$
F12.6	14.707 (1)	14.7049	14.7152	0.0103	. . .	. . .	0.28	0.15	0.15	0.16	$\frac{1}{2} \to \frac{1}{2}$	$2s2p_{1/2}^2 2p_{3/2}^3 3d_{5/2} \to 2s2p^6$
F12.7	14.676 (1)	14.6808	14.6878	0.0070	. . .	. . .	0.33	0.05	0.05	0.05	$\frac{3}{2} \to \frac{1}{2}$	$2s^2 2p_{1/2} 2p_{3/2}^3 3d_{3/2} \to 2s^2 2p_{1/2}^2 2p_{3/2}^4$
F12.8	14.615 (2)	14.6152	14.6241	0.0089	. . .	. . .	0.29	0.06	0.06	0.07	$\frac{3}{2} \to \frac{1}{2}$	$2s^2 2p_{1/2} 2p_{3/2}^3 3d_{5/2} \to 2s^2 2p_{1/2}^2 2p_{3/2}^4$
F13	14.588 (2)	14.5917	14.6809	0.0108	14.616 (10)	14.588	0.20	0.08	0.08	0.09	$\frac{1}{2} \to \frac{3}{2}$	$2s^2 2p_{1/2} 2p_{3/2}^3 3d_{5/2} \to 2s^2 2p_{1/2}^2 2p_{3/2}^3$
F13.1	14.582 (1)	14.5800	14.5922	0.0122	. . .	. . .	0.54	0.29	0.29	0.32	$\frac{3}{2} \to \frac{1}{2}$	$2s2p_{1/2}2p_{3/2}^4 3d_{3/2} \to 2s2p^6$
F14	14.554 (1)	14.5578	14.5655	0.0077	14.571 (11)	14.555	0.41	0.20	0.20	0.22	$\frac{3}{2} \to \frac{3}{2}$	$2s^2 2p_{1/2} 2p_{3/2}^3 3d_{5/2} \to 2s^2 2p_{1/2}^2 2p_{3/2}^3$
F15	14.540 (1)	14.5395	14.5486	0.0091	14.534 (3)	14.540	0.53	0.36	0.36	0.38	$\frac{5}{2} \to \frac{3}{2}$	$2s^2 2p_{1/2} 2p_{3/2}^3 3d_{5/2} \to 2s^2 2p_{1/2}^2 2p_{3/2}^3$
F15.1	14.486 (2)	14.4894	14.4963	0.0069	. . .	. . .	0.23	0.03	0.03	0.03	$\frac{3}{2} \to \frac{3}{2}$	$2s^2 2p_{1/2} 2p_{3/2}^3 3d_{3/2} \to 2s^2 2p_{1/2}^2 2p_{3/2}^3$
F15.2	14.470 (2)	14.4689	14.4802	0.0113	. . .	. . .	0.30	0.04	0.04	0.05	$\frac{1}{2} \to \frac{1}{2}$	$2s2p_{1/2}2p_{3/2}^4 3d_{3/2} \to 2s2p^6$
F15.3	14.457 (2)	14.4637	14.5121	0.0484	. . .	. . .	0.30	0.06	0.06	0.06	$\frac{5}{2} \to \frac{3}{2}$	$2s2p_{1/2}2p_{3/2}^4 3d_{5/2} \to 2s^2 2p_{1/2}^2 2p_{3/2}^3$
F15.4	14.436 (1)	14.4294	14.4374	0.0080	. . .	. . .	0.29	0.05	0.05	0.06	$\frac{3}{2} \to \frac{3}{2}$	$2s2p_{1/2}2p_{3/2}^4 3d_{5/2} \to 2s^2 2p_{1/2}^2 2p_{3/2}^3$
F16	14.420 (2)	14.4151	14.4263	0.0112	14.425 (9)	14.422	0.71	0.09	0.09	0.13	$\frac{3}{2} \to \frac{1}{2}$	$2s^2 2p_{1/2} 2p_{3/2}^3 3d_{5/2} \to 2s^2 2p_{1/2}^2 2p_{3/2}^4$
F16.1	14.388 (1)	14.4000	14.4091	0.0091	. . .	. . .	0.54	0.01	0.01	0.01	$\frac{3}{2} \to \frac{3}{2}$	$2s^2 2p_{1/2} 2p_{3/2}^3 3d_{5/2} \to 2s^2 2p_{1/2}^2 2p_{3/2}^3$
F17	14.377 (1)	14.3768	14.3862	0.0094	14.373 (6)	14.378	0.82	0.44	0.44	0.46	$\frac{5}{2} \to \frac{3}{2}$	$2s2p_{1/2}2p_{3/2}^4 3d_{3/2} \to 2s^2 2p_{1/2}^2 2p_{3/2}^3$
F18	14.368 (1)	14.3514	14.3638	0.0124	14.343 (10)	14.360	0.76	0.47	0.47	0.49	$\frac{3}{2} \to \frac{1}{2}$	$2s2p_{1/2}2p_{3/2}^4 3d_{3/2} \to 2s^2 2p_{1/2}^2 2p_{3/2}^4$
F18.1	14.348 (1)	14.3398	14.3533	0.0135	. . .	. . .	0.60	0.32	0.32	0.35	$\frac{1}{2} \to \frac{1}{2}$	$2s2p_{1/2}2p_{3/2}^4 3d_{5/2} \to 2s^2 2p_{1/2}^2 2p_{3/2}^4$
F19	14.257 (1)	14.2610	14.2693	0.0083	. . .	. . .	0.62	0.09	0.09	0.11	$\frac{5}{2} \to \frac{3}{2}$	$2s2p_{1/2}2p_{3/2}^4 3d_{5/2} \to 2s^2 2p_{1/2}^2 2p_{3/2}^3$
F19	14.257 (1)	14.2579	14.2719	0.0140	14.256 (5)	14.260	0.62	0.27	0.27	0.29	$\frac{1}{2} \to \frac{3}{2}$	$2s2p_{1/2}2p_{3/2}^4 3d_{3/2} \to 2s^2 2p_{1/2}^2 2p_{3/2}^3$
F20	14.206 (1)	14.2057	14.2070	0.0013	14.208 (3)	. . .	0.81	0.64	0.64	0.65	$\frac{3}{2} \to \frac{3}{2}$	$2s2p_{1/2}2p_{3/2}^4 3d_{5/2} \to 2s^2 2p_{1/2}^2 2p_{3/2}^3$
F20	14.201 (1)	14.1949	14.1562	0.0387	14.208 (3)	14.212	1.00	1.00	1.00	1.00	$\frac{5}{2} \to \frac{3}{2}$	$2s2p_{1/2}2p_{3/2}^4 3d_{3/2} \to 2s^2 2p_{1/2}^2 2p_{3/2}^3$
F20.1	14.181 (2)	14.1662	14.1774	0.0112	. . .	. . .	0.42	0.18	0.18	0.20	$\frac{3}{2} \to \frac{1}{2}$	$2s2p_{1/2}^2 2p_{3/2}^3 3d_{5/2} \to 2s2p^6$
F21	14.150 (3)	14.1486	14.1589	0.0103	14.158 (15)	14.154	0.54	0.10	0.10	0.12	$\frac{3}{2} \to \frac{1}{2}$	$2s2p_{1/2}2p_{3/2}^4 3d_{3/2} \to 2s2p^6$
F21	14.150 (3)	14.1460	14.1580	0.0120	. . .	. . .	0.54	0.14	0.14	0.16	$\frac{1}{2} \to \frac{1}{2}$	$2s2p_{1/2}2p_{3/2}^4 3d_{3/2} \to 2s2p^6$
F21.1	14.134 (2)	14.1438	14.2171	0.0733	. . .	. . .	0.34	0.11	0.11	0.14	$\frac{3}{2} \to \frac{3}{2}$	$2s^2 2p_{1/2} 2p_{3/2}^3 3d_{3/2} \to 2s^2 2p_{1/2}^2 2p_{3/2}^3$
F21.2	14.131 (6)	14.1326	14.1462	0.0136	. . .	. . .	0.42	0.06	0.06	0.08	$\frac{1}{2} \to \frac{3}{2}$	$2s^2 2p_{1/2} 2p_{3/2}^3 3d_{5/2} \to 2s^2 2p_{1/2}^2 2p_{3/2}^3$
F21.3	14.119 (3)	14.0780	14.0864	0.0084	. . .	. . .	0.64	0.41	0.41	0.45	$\frac{3}{2} \to \frac{1}{2}$	$2s^2 2p_{3/2}^4 3d_{3/2} \to 2s^2 2p_{1/2} 2p_{3/2}^4$
F22	13.954 (2)	13.9142	13.9235	0.0093	13.953 (11)	13.960	0.43	0.11	0.11	0.12	$\frac{5}{2} \to \frac{3}{2}$	$2s^2 2p_{3/2}^4 3d_{5/2} \to 2s^2 2p_{1/2} 2p_{3/2}^3$

NOTES.—A "b" after the label indicates a blend. Labels correspond to the notation of Brown et al. (2002). "A"—Model A: optically thin. "B"—Model B: optically thin and EA/DR. "C"—Model C: optically thick and EA/DR. Models conditions were $n_e = 10^{21}$ cm^{-3} and $T_e = 200$ eV.

[a] Brown et al. (2002).
[b] Phillips et al. (1999, 1982).

TABLE 7
PREDICTED AND IDENTIFIED BRIGHT LINES OF Fe XIV (O-LIKE)

Label	λ_{exp} (Å)	λ_{HUL} (Å)	λ_{Brown}[a] (Å)	$\lambda_{Phillips}$[b] (Å)	I_{ENEA}	I_{HUL} (A)	I_{HUL} (B)	I_{HUL} (C)	$J_{upper} \rightarrow J_{lower}$	Configuration
O0.1	16.936 (1)	16.9887	...	...	1.00	0.00	0.00	0.00	$2 \rightarrow 1$	$2s^22p_{1/2}2p_{3/2}^23p_{3/2} \rightarrow 2s2p_{1/2}2p_{3/2}^4$
...	...	14.9968	...	...	...	0.25	0.25	0.25	$2 \rightarrow 2$	$2s^22p_{1/2}2p_{3/2}^23s \rightarrow 2s^22p_{1/2}2p_{3/2}^3$
O13	14.694 (1)	14.6687	14.664 (7)	14.670	0.46	0.32	0.32	0.32	$3 \rightarrow 2$	$2s^22p_{1/2}2p_{3/2}^23s \rightarrow 2s^22p_{1/2}^22p_{3/2}^2$
...	...	13.9462	...	...	...	0.28	0.28	0.28	$3 \rightarrow 2$	$2s2p_{1/2}2p_{3/2}^34s \rightarrow 2s2p_{1/2}^22p_{3/2}^3$
O20	13.798 (1)	13.7904	13.759 (5)	13.792	0.46	0.41	0.41	0.41	$3 \rightarrow 2$	$2s^22p_{1/2}2p_{3/2}^23d_{5/2} \rightarrow 2s^22p_{1/2}^22p_{3/2}^2$
O20.1	13.778 (1)	13.7893	...	13.780	0.33	0.28	0.28	0.28	$2 \rightarrow 2$	$2s^22p_{1/2}2p_{3/2}^23d_{5/2} \rightarrow 2s^22p_{1/2}2p_{3/2}^3$
O20.2	13.748 (1)	13.7239	...	...	0.43	0.44	0.44	0.44	$3 \rightarrow 2$	$2s^22p_{1/2}^22p_{3/2}3d_{5/2} \rightarrow 2s^22p_{1/2}2p_{3/2}^3$
O20.3	13.716 (1)	13.7072	...	...	0.41	0.36	0.36	0.36	$2 \rightarrow 1$	$2s^22p_{1/2}2p_{3/2}^23d_{5/2} \rightarrow 2s^22p_{1/2}2p_{3/2}^3$
...	...	13.6569	...	...	...	0.19	0.19	0.19	$1 \rightarrow 1$	$2s^22p_{1/2}2p_{3/2}^23d_{5/2} \rightarrow 2s^22p_{1/2}2p_{3/2}^3$
...	...	13.6434	...	...	...	0.22	0.22	0.22	$3 \rightarrow 2$	$2s^22p_{1/2}2p_{3/2}^23d_{3/2} \rightarrow 2s^22p_{1/2}^22p_{3/2}^2$
...	...	13.6404	...	...	...	0.20	0.20	0.21	$2 \rightarrow 1$	$2s2p_{3/2}^43d_{3/2} \rightarrow 2s2p_{1/2}2p_{3/2}^4$
...	...	13.5727	...	...	...	0.21	0.21	0.21	$3 \rightarrow 2$	$2s2p_{1/2}2p_{3/2}^33d_{5/2} \rightarrow 2s2p_{1/2}^22p_{3/2}^3$
...	...	13.5127	...	...	...	0.91	0.91	0.91	$3 \rightarrow 2$	$2s^22p_{1/2}2p_{3/2}^23d_{5/2} \rightarrow 2s^22p_{1/2}^22p_{3/2}^2$
...	...	13.4976	...	...	...	0.60	0.60	0.60	$2 \rightarrow 2$	$2s^22p_{1/2}2p_{3/2}^23d_{3/2} \rightarrow 2s^22p_{1/2}^22p_{3/2}^2$
...	...	13.4863	...	...	...	1.00	1.00	1.00	$3 \rightarrow 2$	$2s^22p_{3/2}^33d_{3/2} \rightarrow 2s^22p_{1/2}2p_{3/2}^3$
...	...	13.4853	...	...	...	0.32	0.32	0.32	$2 \rightarrow 2$	$2s^22p_{3/2}^33d_{3/2} \rightarrow 2s^22p_{1/2}2p_{3/2}^3$
...	...	13.4849	...	...	...	0.23	0.23	0.23	$2 \rightarrow 1$	$2s^22p_{1/2}2p_{3/2}^23d_{5/2} \rightarrow 2s^22p_{1/2}2p_{3/2}^3$
...	...	13.4596	...	...	...	0.31	0.31	0.31	$1 \rightarrow 2$	$2s^22p_{1/2}2p_{3/2}^23d_{3/2} \rightarrow 2s^22p_{1/2}^22p_{3/2}^2$
...	...	13.4233	...	...	...	0.04	0.04	0.04	$2 \rightarrow 1$	$2s2p_{1/2}^22p_{3/2}3d_{5/2} \rightarrow 2s2p_{1/2}^22p_{3/2}^2$
...	...	13.4095	...	...	...	0.22	0.22	0.22	$3 \rightarrow 2$	$2s^22p_{1/2}^22p_{3/2}3d_{5/2} \rightarrow 2s^22p_{1/2}^22p_{3/2}^2$
...	...	13.4040	...	...	...	0.23	0.23	0.23	$1 \rightarrow 1$	$2s^22p_{3/2}^33d_{3/2} \rightarrow 2s^22p_{1/2}2p_{3/2}^3$

NOTES.—A "b" after the label indicates a blend. Labels correspond to the notation of Brown et al. (2002). "A"—Model A: optically thin. "B"—Model B: optically thin and EA/DR. "C"—Model C: optically thick and EA/DR. Models conditions were $n_e = 10^{21}$ cm^{-3} and $T_e = 200$ eV.
[a] Brown et al. (2002).
[b] Phillips et al. (1999, 1982).

TABLE 8
CONFIGURATIONS INCLUDED IN HULLAC MODELING

CHARGE STATE	ISOELECTRONIC SEQUENCE	MAIN ION Configurations	MAIN ION Configuration Range	COUPLED ION FOR EA/DR Configurations	COUPLED ION FOR EA/DR Configuration Range
Fe XX	N-like	...	...	$2s^22p^3$ $2s^22p^23l$	$l = s, p, d$
Fe XIX	O-like	$2s^22p^4$ $2s2p^5$ $2p^6$ $2s^22p^3nl$ $2s2p^4nl$	 $n = 3, 4, 5, l = s, p, d, f, g$ $n = 3, 4, 5, l = s, p, d, f, g$	$2s^22p^4$ $2s^22p^33l$	$l = s, p, d$
Fe XVIII	F-like	$2s^22p^5$ $2s2p^6$ $2s2p^55nl$ $2s^22p^4nl$	 $n = 3, 4, 5, l = s, p, d, f, g$ $n = 3, 4, 5, l = s, p, d, f, g$	$2s^22p^5$ $2s^22p^43l$	$l = s, p, d$
Fe XVII	Ne-like	$2s^22p^6$ $2s^22p^5nl$ $2s2p^6nl$	 $n = 3, 4, 5, l = s, p, d, f, g$ $n = 3, 4, 5, l = s, p, d, f, g$	$2s^22p^6$ $2s^22p^53l$	$l = s, p, d$
Fe XVI	Na-like	$2s^22p^6nl$ $2s^22p^53l'nl$ $2s2p^63l'nl'$	$n = 3, 4, 5$ $n = 3, 4, 5, l' = s, p, d, l = s, p, d, f, g$ $n = 3, 4, 5, l' = s, p, d, l = s, p, d, f, g$	$2s^22p^63l$	$l = s, p, d$
Fe XVII	Mg-like	$2s^22p^63l3l'$ $2s^22p^63snl$ $2s^22p^53l3l'3l''$ $2s^22p^53s3l'nl$ $2s2p^63l3l'3l''$ $2s2p^63s3l'nl$	$l = s, p, d, l' = s, p, d$ $n = 4, 5, l = s, p, d, f, g$ $l, l', l'' = s, p, d$ $n = 4, 5, l' = s, p, d, l = s, p, d, f, g$ $l, l', l'' = s, p, d$ $n = 4, 5, l' = s, p, d, l = s, p, d, f, g$	...	...

with those of the adjacent ionization states. For model B, the level populations of each ionization state were coupled with those of the higher charged ion. The structure of the higher charged ion included fewer levels as detailed in Table 8. The smaller models included the necessary states for EA/DR and reduced the computational time to a reasonable level. Dielectronic recombination rate coefficients were determined by requiring detailed balance of the HULLAC autoionization rates. For model C, the level populations were coupled as was done in model B. Additionally, a plasma length of 200 μm was used to correct the line intensities for an optically thick high-density plasma (Fournier et al. 2003b).

All electric and magnetic dipole and quadrupole radiative transitions (E1, M1, E2, and M2) were included in the modeling. The rate coefficients and the radiative transition probabilities were put into a collisional-radiative matrix. The level populations were calculated by solving the coupled set of equations:

$$\frac{dn_j}{dt} = 0 = \sum_{i \neq j} n_i R_{i \to j} - n_j \sum_{i \neq j} R_{j \to i},$$

where n_i is the relative population of level i of a given ion, $R_{j \to i}$ is the rate at which population transfers from level j to level i, which can be in the adjacent ionization state. The relative emissivity, $J_{i \to j}$, for each transition within an ionization state was calculated for a Maxwell-Boltzmann temperature of 200 eV and a density of 1×10^{21} cm^{-3}. Tables 3–7 list the relative intensities for the brighter lines in a given ionization state for all the models considered in this paper. Intensities are normalized to the brightest line in the region. Each intensity was convoluted with a Gaussian line width function with a $\Delta\lambda_{\mathrm{FWHM}}$ of 15 mÅ to produce the synthetic spectrum.

The laser plasmas contained several charge states of iron. A charge state distribution (CSD) was required both to determine the effect of EA/DR on the line intensities and to determine the relative intensity of the lines of the different ions. HULLAC could not calculate an accurate CSD. For the calculations of the effect of EA/DR on the line intensities, the relative fractions of O-like to F-like iron were assumed to be those predicted by Arnaud & Raymond (1992, hereafter AR92) for a plasma at 200 eV. For the relative ratio of the different ionization states of iron, the CSD was treated as a free parameter and was deter-
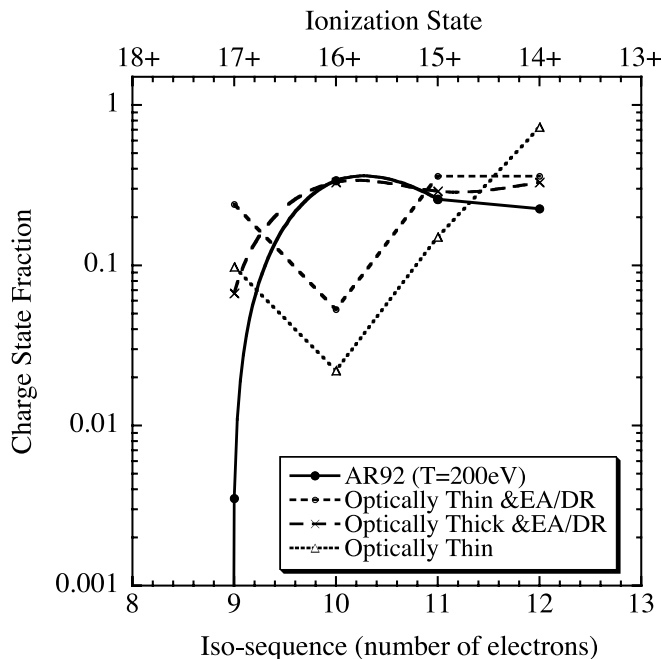
Fig. 3.—Iron charge state distributions derived from fitting the three separate models to the Hercules plasma spectrum and the predictions of AR92 at $T_e = 200$ eV and $n_e = 1 \times 10^{21}$ cm^{-3}.

mined from fitting the measured spectra (Fig. 3 and Table 9). The resultant CSD from the fits was found to be both a reasonable choice and relatively consistent with AR92.

In addition to the HULLAC calculations, the Flexible Atomic Code (FAC) was used to calculate the transition wavelengths for both the Ne-like and F-like iron ions. Details of the FAC code are given in Gu (2004). The calculated wavelengths are given in Tables 5 and 6. Comparing these two predictions provided a level of uncertainty on the calculated wavelengths from the atomic structure codes.

6. IDENTIFICATION OF SPECTRAL LINES

Spectra from all three laser-produced plasmas (TVG, ENEA, and COMET) were utilized to identify the Fe lines. The plasmas produced had different characteristics (e.g., energy density, pulse

TABLE 9
CSD Predicted by Arnaud & Raymond (1992) for Different Temperatures and the CSD Derived
from the Fitting of the Three HULLAC Models to the Hercules Spectrum

Temperature (keV)	O-like	F-like	Ne-like	Na-like	Mg-like
0.150..............................	1.24E−08	4.27E−05	0.0306	0.0508	0.145
0.200..............................	1.20E−05	0.00350	0.337	0.259	0.225
0.250..............................	0.000295	0.0196	0.570	0.268	0.111
0.300..............................	0.00230	0.053	0.668	0.216	0.051
Experiment and Fit with Model A: Optically Thin no EA/DR					
...		0.098	0.022	0.15	0.73
Experiment and Fit with Model B: Optically Thin with EA/DR					
...		0.24	0.053	0.36	0.36
Experiment and Fit with Model C: Optically Thick with EA/DR					
...		0.067	0.33	0.29	0.33
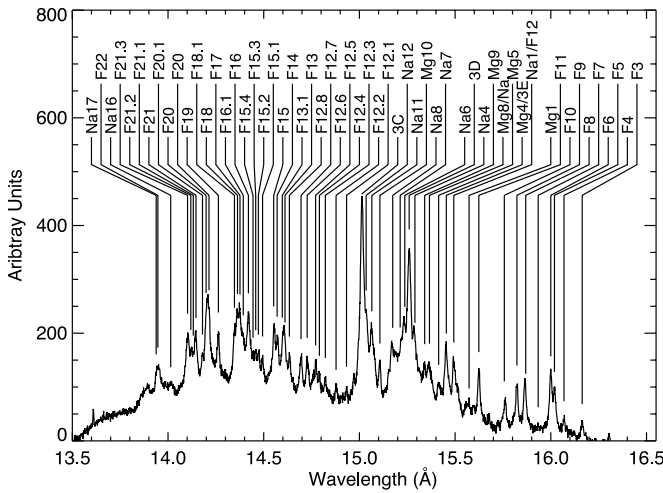
FIG. 4.—COMET spectrum created with line identifications. The first laser beam was 600 ps with 4 J. The second laser beam occurred 1.4 ns later and was 1.2 ps with 4.8 J.

duration, etc.) and produced different spectra of the Fe XIV to Fe XIV ions. This yielded a good understanding of the measured spectral lines. The recorded spectra evolved from the lower ionization states, Na-like and Mg-like, up to the higher ionization states, O-like, in the best focused and highest energy density plasmas (Fig. 1). Many of the recorded Na- and Mg-like lines are dielectronic satellites. By using the spectra from the TVG, ENEA, and COMET experiments and HULLAC modeling the identification of a line was determined.

The identifications of the spectral lines were done through comparisons with the HULLAC modeling and with the work of Brown et al. (1998, 2002) for the O-like, F-like, and Ne-like lines. The Na-like and Mg-like lines were identified through comparisons only with the HULLAC modeling. The relative level of accuracy of the wavelength calculations was good enough to associate a given measured line to a predicted atomic transition. For most of the O-like, F-like, and Ne-like lines, the identifications were straightforward. The identifications of the Na-like and Mg-like lines were more difficult. Even with the high-resolution spectra, many of the lines from these charge states were difficult to identify due to line blending. Both the wavelengths and the relative intensities were used to identify the Na- and Mg-like lines. The line labels follow the convention of Brown et al. (1998, 2002) Since more lines were observed in the high-density plasma than the low-density plasma, the lines not observed by Brown et al. are indicated by "ZX.Y." The letter "Z" is the isosequence (O, F, etc), and "X.Y" is the numerical identifier. The identifications are listed in the tables. We present in Figure 4 a spectrum recorded from COMET between 13.5 and 16.5 Å of the F-like to Mg-like iron lines with identifications.

Brown et al. identified a number of these lines in the low-density plasma. However, the atomic processes in high-density plasmas (e.g., EA, DR, etc.) enhanced or reduced the relative intensities of different lines. We recorded many Na- and Mg-like iron lines that were not recorded by Brown et al. The spectral resolution of the measurements by Brown et al. was $\lambda/\Delta\lambda \approx 500$. The higher resolution of our measurements allowed us to split several lines that Brown could not resolve (e.g., F20) and to record a detailed spectrum of the closely spaced Na-like and Mg-like lines. From the TVG spectra in Figure 1, it is clearly seen that a high spectral resolution up to ≈ 4000 was achieved for the iron spectra in vicinity of resonance lines of Ne-like iron.

The two Ne-like Fe XVII $3d \rightarrow 2p$ 3C and 3D resonance lines at 15.014 and 15.267 Å corresponding to the $2p^53d \rightarrow 2p^6$ ($^1P_1 \rightarrow {}^1S_0$) and $2p^53d \rightarrow 2p^6$ ($^3P_1 \rightarrow {}^1S_0$) transitions, respectively, have a lower observed spectral resolution ($\lambda/\Delta\lambda = 1200$–1500) than the surrounding satellite lines as a result of the strong optical absorption of the plasma.

The identified lines of iron are compared with the wavelength calculations of HULLAC and measurements by Brown et al. (1998, 2002) and Phillips et al. (1999, 1982). Wavelengths for Mg-like to O-like iron are given in Tables 3–7, respectively. The calculated HULLAC X-ray transition wavelengths differed by less than ≈ 20 mÅ from the measured wavelengths for most lines in all the charge states studied with a few differences above 50 mÅ. The HULLAC X-ray transition wavelengths differed from the calculated FAC wavelengths by ≈ 10 mÅ and were on average closer to our measured values than the FAC calculations for F-like and Ne-like iron. Gu (2005) in a recent publication calculated energy levels and wavelengths of Fe and Ni ions using a combined configuration interaction and many-body perturbation theory approach. This is a more sophisticated calculation than that done by HULLAC or FAC. Some of Gu's wavelengths are in slightly better agreement with our experiment than the HULLAC and FAC calculations reported in this paper. Our experimental wavelengths were on average less than 8 mÅ from the wavelengths measured by Brown et al. A similar difference is found between our measurements and those of Phillips et al. This difference is considerably larger than the respective error limits, including our error limits, which are typically 1–3 mÅ. The reason for this may be that some lines are blended with satellite transitions that shift the apparent wavelength of a given line. This is likely given the high density of lines in our laser-produced spectra.

7. SPECTRAL INTENSITIES

The spectra recorded from the Hercules iron plasmas were compared with the synthetic spectra from HULLAC. This plasma was chosen since it was the least complex plasma to model. The optical thickness was thought to be the smallest. Moreover, the ENEA plasma did not have the complexity of the multibeam COMET plasma.
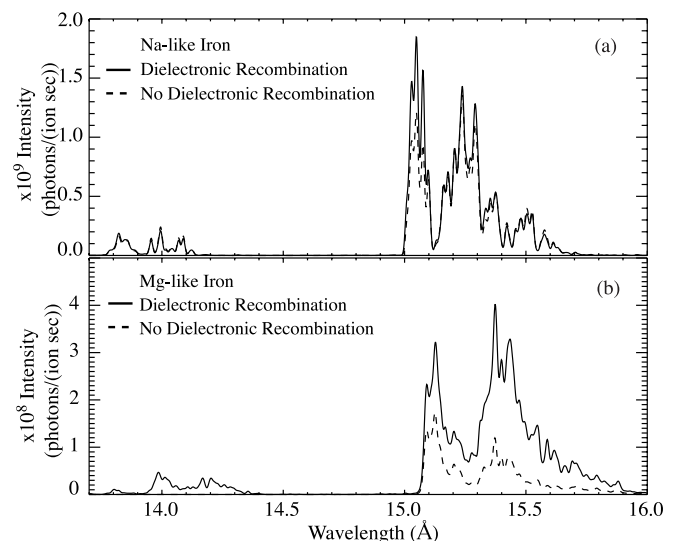
FIG. 5.—Comparison of Na-like and Mg-like iron HULLAC simulations with and without including the effects of EA/DR on the line intensities ($T_e = 200$ eV, $n_e = 1 \times 10^{21}$ cm^{-3}).
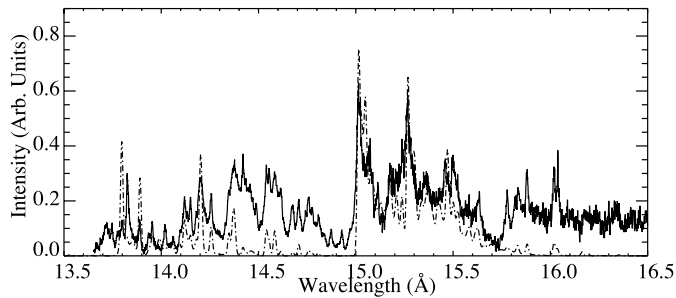
Fig. 6.—Iron spectrum from the plasma created by the Hercules laser (*solid line*) and the fits of the HULLAC simulation (*dashed line*) at $T_e = 200$ eV and $n_e = 1 \times 10^{21}$ cm^{-3} using model C.

The three HULLAC models predicted different spectra due to the different processes included in each. The addition of EA/DR to model B (optically thin model) significantly affected the line intensities of the Na- and Mg-like iron lines as can be see in Figure 5. The calculated intensities significantly increased when EA/DR was included in the modeling but did not significantly alter the overall shape of the emission. The Na-like ion line intensities increased ≈50% for the lines on the red side of the 3C line and ≈10% for the lines on the red side of the 3D line. For Mg-like iron, the line intensities on the red side of the 3C line are doubled, and the intensities on the red side of the 3D are almost quadrupled. The intensities for the lines between 14.0 and 14.5 Å for Na-like were unaffected by DR, but the Mg-like line intensities increased by a factor of ≈100. DR did not appreciably alter the simulated line intensities of the Ne-like, F-like, and O-like iron ions.

Model C calculated the line intensities assuming an optically thick (OT) plasma that also included the effects of EA/DR. The optically thick plasma had a significant impact on the more intense lines of Ne-like, Na-like, and Mg-like iron. For Ne-like iron, the most dramatic change was a decrease of approximately a factor of 10 in the 3C and 3D line intensities. Model C accurately reproduced the measured intensities for the Ne-like ion (Table 5). The most intense Na-like, Mg-like, and F-like iron lines in the simulation were reduced by roughly a factor of 4, 2, and 1.5, respectively, compared to the optically thin simulation, model B.

The three HULLAC models were fitted to the Hercules spectra. The free parameter in the fitting is the CSD. The spectral fit is shown in Figure 6 for model C. The resulting CSDs derived from this analysis and predicted values from AR92 for astrophysical plasmas are given in Table 9 and Figure 3. For the optically thin model with no DR, the charge balance is very hollow and not realistic. With the addition of the DR, the CSD looks more realistic except for the very small Ne-like fraction. Model C reproduced the measured spectrum the best, yielded the most realistic CSD, and agreed with AR92. The laser plasmas have a much higher density than AR92. The AR92 calculations are a low-density limit calculation and assume three-body processes and photoabsorption are negligible. Our CSDs should be considered an upper bound on the temperature since higher density plasmas are more ionized than lower density plasmas at the same temperature. We conclude that the plasma temperature is ≤200 eV, and the electron density is ≈10^{21} cm^{-3}. These are consistent with the findings of Vergunova et al. from K-shell spectra.

The HULLAC modeling is good but does not fully reproduce every feature in the recorded spectra. The average discrepancy between the measured and the synthetic intensities of the iden-

tified bright lines was ≈50%. The Na-like and Mg-like features are well simulated but are blended with the Ne-like lines. Between 14 and 15 Å, there are many missing lines in F-like spectra. The O0.1 line at 16.936 Å is the brightest O-like line that was recorded; however, HULLAC does not predict this feature to have any appreciably intensity.

8. CONCLUSIONS

Iron spectra have been recorded at three different laser plasma facilities: the Tor Vergata University laser in Rome (Italy), the Hercules laser at ENEA in Frascati (Italy), and the Compact Multipulse Terawatt (COMET) laser at LLNL in California (USA). The laser plasmas had electron temperatures between 100 and 500 eV and electron densities between 10^{20} and 10^{22} cm^{-3}. The $\Delta n \geq 1$ lines of Fe xv (Mg-like) to Fe xiv (O-like) were recorded between 13.8 and 17.1 Å with high spectral resolution ≈4000. The Hebrew University Lawrence Livermore Atomic Code was used to calculate the atomic structure and atomic rates. Identification of these lines were done through comparisons with HULLAC modeling and previous works of Brown et al. Accurate wavelength measurements were determined for ≈80 emission lines from the recorded spectrum. The majority of the calculated HULLAC X-ray transition wavelengths differed by less than ≈20 mÅ from the measured wavelengths for most lines with a few differences above 50 mÅ. For most of the lines, the differences between our measurements and previous measurements were less than ≈8 mÅ. HULLAC calculated synthetic line intensities for three different conditions: optically thin plasmas with no contribution of EA/DR to the line intensities, optically thin plasmas that included EA/DR contributions to the line intensities, and optically thick plasmas that included EA/DR contributions to the line intensities. These simulations were fitted to the recorded spectra from the Hercules laser. The CSD was a free parameter. The optically thick simulation best reproduced the recorded spectrum and provided the most realistic CSD. From this we concluded that this plasma had a temperature of ≤200 eV plasma. The Na-like and Mg-like features near the 3C and 3D emission lines were well reproduced by the HULLAC modeling. The 3C and 3D lines are blended with Na-like and Mg-like features. However, the emission features between 14 and 15 Å were not well simulated. Some significant omissions in the F-like HULLAC models did exist.

The present measurement provides wavelengths for nearly 30 Fe xv and Fe xvi transitions that have not yet been identified in low-density, coronal plasmas. The transitions are mainly populated by dielectronic recombination. Although dielectronic recombination is less important in the low-density electron beam ion trap plasma, this process is active and produces weak features that enhance the background level near the Fe xvii 3C, 3D, and 3E lines. Our lines should aid in improving the modeling of these dielectronic satellites and thus increasing the accuracy with which the intensity of the Fe xvii lines can be inferred from observation.

REFERENCES

Arnaud, M., & Raymond, J. 1992, ApJ, 398, 394

Bar-Shalom, A., Klapisch, M., & Oreg, J. 2001, J. Quant. Spectrosc. Radiat. Transfer, 71, 169

Behar, E., Cottam, J., & Kahn, S. M. 2001, ApJ, 548, 966

Boiko, I., Pal'chikov, V. G., Skobelev, I. Yu., & Faenov, A. Ya. 1994, Spectroscopic Data of Atoms and Ions (Atom Spectra with One and Two Electrons (Boca Raton: CRC Press)

Bollanti, S., Lazzaro, P. Di, Flora, F., Letardi, T., Palladino, L., Reale, A., Batani, D., Mauri, A., Scafati, A., Grilli, A., Faenov, A. Ya., Pikuz, T. A., Pikuz, S. A., & Osterheld, A. 1995, Phys. Scr., 51, 326

Bollanti, S., et al. 1996, Nuovo Cimento D, 18, 1241

Brown, G. V., Beiersdorfer, P., Chen, H., Chen, M. H., & Reed, K. J. 2001, ApJ, 557, L75

Brown, G. V., Beiersdorfer, P., Liedhal, D. A., Widmann, K., & Kahn, S. M. 1998, ApJ, 502, 1015

———. 2002, ApJS, 140, 589

Brunetkin, B. A., Pikuz, S. A., Skobelev, I. Yu., Faenov, A. Ya. Khabibylaev, B. K., & Ermatov, Sh.A 1992, Soviet J. Quantum Electron., 22, 9, 853

Drake, G. W. 1988, Canadian J. Phys., 66, 586

Dunn, J., Nilsen, J., Osterheld, A. L., Li, Y., & Shlyaptsev, V. N. 1999, Opt. Lett., 24, 101

Faenov, A. Ya., et al. 1994, Phys. Scr., 50, 333

Fournier, K. B., et al. 2003a, J. Phys. B, 36, 3787

———. 2003b, Phys. Rev. E, 67, 016402

Garcia, J. D., & Mack, J. E. 1963, J. Opt. Soc. Am., 55, 654

Gu, M. F. 2004, Proc. 14th APS Topical Conference on Atomic Processes in Plasmas, 730, 127

Gu, M. F. 2005, ApJS, 156, 105

Henke, B. L., Fujiwara, F. G., Tester, M. A., Dittmore, C. H., & Palmer, M. A. 1984, J. Opt. Soc. Am., 1, 828

Lazzaro, P. D. 1998, Proc. SPIE, 3423, 35

Magunov, H. I., Faenov, A. Ya., Skobelev, I. Yu., & Pikuz, T. A. 1995, Ray-Tracing Code for FSSR Spectrometers, VNIIFTRI

Phillips, K. J. H., Mewe, R., Harra-Murnion, L. K., Kaastra, J. S., Beiersdorfer, P., Brown, G. V., & Liedahl, D. A. 1999, A&AS, 138, 381

Phillips, K. J. H., et al. 1982, ApJ, 256, 774

Pikuz, T. A., Faenov, A. Ya., Pikuz, S. A., Romanova, V. M., & Shelkovenko. T. A. 1995, J. X-ray Sci. Technol., 5, 323

Skobelev, I. Yu., Faenov, A. Ya., Bryunetkin, B. A., Dyakin, V. M, Pikuz, T. A., Pikuz, S. A., Shelkovenko, T. A., & Romanova, V. M. 1995, JETP, 81, 692

Vergunova, G. A., et al. 1997, Phys. Scr., 55, 483

Young, B. K., et al. 1998, Rev. Sci. Instrum., 69, 4049